

EXTRACTION OF LINEAR INFLOW MODEL FOR MANEUVERING HELICOPTER FROM FREE-WAKE ANALYSIS

Omri Rand, Vladimir Khromov

Faculty of Aerospace Engineering

Technion - Israel Institute of Technology, Haifa, Israel

Keywords: *Dynamic Inflow, Coaxial Rotor, State-Space Dynamics, Maneuvering Flight*

Abstract

The paper describes a methodology which is founded on a Single Frequency Analysis to extract a linearized state-space dynamic inflow model from a generic and high fidelity aerodynamic analysis for single and coaxial helicopter rotor systems. The methodology is computationally efficient and provides the entire frequency-domain behavior of the wake inflow states. The paper also includes an extension of the methodology to the case of heaving, rolling and pitching rotor disc.

1 Introduction

Linear inflow models are widely used and are an essential tool for real-time helicopter simulation tasks of both full-scale and UAV configurations. These models also play a major role in flight control systems design and in evaluation processes of compliance with handling qualities specifications. Basically, dynamic inflow models are derived in the frequency domain and thereafter support time-domain applications that utilize their state-space form.

Linear inflow models were traditionally based on analytical and semi-analytical models, see e.g. Refs.[1-4]. Nowadays, advanced aerodynamic computational tools such as free wake models and CFD-based numerical procedures are widely used for detailed

modeling and accurate prediction of the flow-fields around generic rotary-wing configurations in various flight regimes. Yet, while such modern tools include fewer theoretical limitations and approximations than the classical and simplified schemes, they are impractical or impossible to be directly applied to many simulation tasks and flight dynamics problems, as they are not formulated in a state-space form and are often computationally intensive. It is therefore desired to develop consistent methodologies that will be capable of utilizing the accuracy provided by advanced tools to improve linear inflow models and subsequently provide more realistic flight dynamics calculations along with simulations of better quality and fidelity, see e.g. Refs.[5-10].

The classical dynamic inflow models are founded on small-disturbances and momentum theory based solutions, which globally represent the rotor inflow dynamics. The most popular models are the Pitt and Peters “dynamic inflow” model Ref.[1], the Peters and He “finite state wake” Ref.[4], and their numerous subsequent developments. These models trace their origins directly to the small disturbances, acceleration potential solution over a disc by Joglekar and Loewy Ref.[11].

The classical models assume small loading perturbations at the rotor disc and their extension to include maneuvering flight requires some assumptions regarding the resulting changes in the wake geometry.

Fundamentally, these are solutions for a single rotor, and therefore their extension to complex interactions associated with multi-rotor configurations, rotor-fuselage or rotor-empennage interactions is not straight-forward. Yet, they provide quality results for many cases and conditions of practical interest.

In previous studies Ref.[12], two systematic, free wake based methodologies to extract dynamic inflow like models were presented for hover. The present paper extends the *Single frequency analysis* methodology to the case of heaving, rolling and pitching rotor disc and to the case of coaxial rotor systems - for more details see Ref.[13].

To understand the main differences between the classical (semi-analytic) dynamic inflow models and the present aerodynamic analysis along with the associate method for extracting the dynamic inflow coefficients, it is worth mentioning here the most two important distinctions between these two approaches. The first difference is quite obvious: Modern computational fluid dynamics based techniques, including free vortex wake models, have far fewer limitations, and represent the state-of-the-art in rotorcraft aerodynamic modeling. It is therefore expected that utilizing such models will provide better prediction quality of the actual physical system behavior. The second difference goes more deeply into the basic definitions of the state-space form of dynamic inflow-type models. In the classical models, the “states” are defined as quantities that are averaged over the disc at each instance, and hence, such states include data that is not solely related to present time. Such a definition is more suitable for relatively slow dynamics. However, in the present model, the states are defined by adopting the Multi-Blade Coordinate Transformation method and are “exact” in the sense that they are directly related (only) to the *current inflow* distribution *along each blade*. Hence, these states may adequately represent any rate of inflow dynamics as they precisely constitute the inflow quantities that are required for loads estimation during simulation.

Although this paper is focused on the results obtained from a specific free-wake model, it

should be stressed again that the present methodology is completely generic and applicable to any advanced aerodynamic modeling.

2 Aerodynamic Modeling

To carry out the present study, RAPID’s (**R**otorcraft **A**nalysis for **P**reliminary **D**esign) free wake model Refs.[10,12-14] has been used. Since the analysis is focused on a generic “outer inflow solution”, the wake is modeled by a single tip vortex per blade (of each rotor). The said tip vortex is discretized with linear segments defined by collocation points that are allowed to drift freely in the velocity field generated by the combination of the free stream velocity, rotor maneuvering speed and the bound and trailed vorticity. The modeling includes semi-empirical models for vortex core and vortex dissipation. Vortex core is implemented via analytical rigid wake core that is smoothly blended into the far Bio-Savart induced velocity. The vortex dissipation model creates a vortex core that grows asymptotically with the wake age. Subsequently, vortex diffusion takes a major role in creating and updating the wake geometry. For more details see Ref. [13].

Figures 1,2 present the wake as it developed over a relatively long roll and pitch maneuvers. As shown, the structures are quite complex. These will be studied in this paper by series of periodic excitations.

3 The Single frequency analysis for a single-rotor

Dynamic Inflow modelling and its influence on various rotor systems has been vastly dealt with, see e.g. Refs.[15-17]. In Ref.[12] we have studied the generic form of the classical “dynamic inflow-type model” for a single rotor. Following the original work of Pitt and Peters Refs.[1], the inflow is assumed to be governed by the follow-

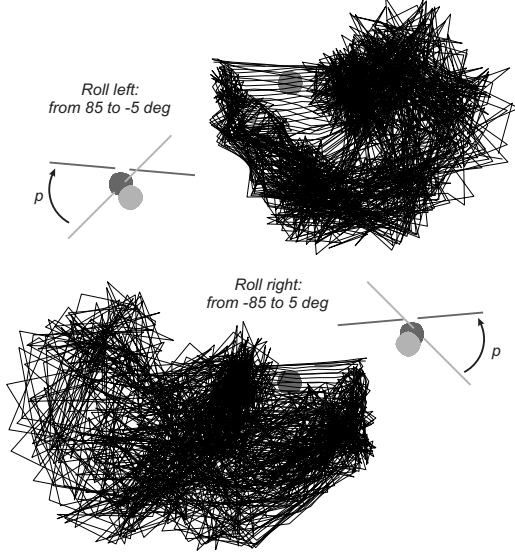


Fig. 1 Wake structure for constant roll, front view ($\mu = 0.07$, $C_T = 0.04$, $\tilde{p} = 0.0125$).

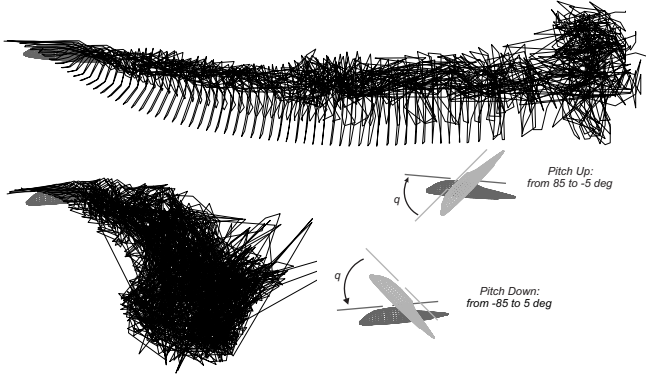


Fig. 2 Wake structure for constant pitch, side view ($\mu = 0.07$, $C_T = 0.04$, $\tilde{q} = 0.0125$).

ing first order dynamics:

$$[M] \begin{pmatrix} * \\ \lambda_0 \\ * \\ \lambda_{1s} \\ * \\ \lambda_{1c} \end{pmatrix} + [L]^{-1} \begin{pmatrix} \lambda_0 \\ \lambda_{1s} \\ \lambda_{1c} \end{pmatrix} = \begin{pmatrix} \Delta C_T \\ \Delta C_L \\ \Delta C_M \end{pmatrix}. \quad (1)$$

In what follows, $[L]^{-1}$ will be denoted as $[\bar{L}]$. The time-history of the rotor loading perturbations is expressed using the azimuth angle of the first blade, namely $\Delta C_T(\psi_1)$, $\Delta C_L(\psi_1)$ and $\Delta C_M(\psi_1)$. These perturbations create a change in the inflow distribution, $\Delta \tilde{v}_i(\psi_1, \tilde{r}, \psi)$. The inflow states λ_0 , λ_{1s} , and λ_{1c} are calculated using the classical linear inflow distribution assumption

as:

$$\Delta \tilde{v}_i(\psi_1, \tilde{r}, \psi) = \lambda_0(\psi_1) + \lambda_{1s}(\psi_1) \tilde{r} \sin(\psi) + \lambda_{1c}(\psi_1) \tilde{r} \cos(\psi), \quad (2)$$

where ψ_1 , the azimuth angle of the first blade, is kept as the main “clock” of the entire solution. Note that the basic hypotheses behind the above formulation are: (i) the system is linear so periodic excitation of the RHS vector of Eq. (1) in a single frequency, say ω , yields a response of λ_0 , λ_{1s} , and λ_{1c} in the same frequency; (ii) the matrices $[M]$ and $[\bar{L}]$ are constants, i.e. not functions of ω . As already indicated, the above assumptions are quite essential for flight dynamics applications and control design, see e.g. Refs.[18-20].

The *Single frequency analysis* is designed to directly extract all elements of the $[M]$ and $[\bar{L}]$ matrices for a given single frequency excitation. Figure 3 summarizes the methodology. As

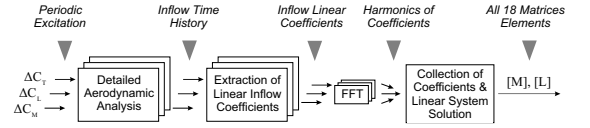


Fig. 3 Scheme of the *Single frequency analysis* methodology for a single rotor system.

shown, following a trim solution, the induced velocity distribution $\tilde{v}_i(\psi_1, \tilde{r}, \psi)$ is determined for various $\Delta C_T(\psi_1)$, $\Delta C_L(\psi_1)$, $\Delta C_M(\psi_1)$ periodic perturbations (one at a time) and the distributions $\Delta \tilde{v}_i(\psi_1, \tilde{r}, \psi) = \tilde{v}_i(\psi_1, \tilde{r}, \psi) - \tilde{v}_{\text{trim}}(\tilde{r}, \psi)$ are evaluated for each perturbation. Linear states time histories ($\lambda_0(\psi_1)$, $\lambda_{1s}(\psi_1)$, $\lambda_{1c}(\psi_1)$) are then extracted. These are FFT analyzed and their cosine and sine components (at the perturbation frequency) $\lambda_0^s, \lambda_0^c, \lambda_{1s}^s, \lambda_{1s}^c, \lambda_{1c}^s, \lambda_{1c}^c$ are obtained. These coefficients are used to determine all 18 $[M]$ and $[\bar{L}]$ coefficients. It should be clarified that the above time history signal consists of additional frequencies which are typically of small amplitude. These are ignored due to the fundamental first order system hypothesis discussed above.

3.1 Creating the Periodic Excitations

In view of the necessity to create a generic model for dynamic inflow that is independent of a specific set of rotor characteristics, a generic relation between the perturbations in hub loads (rotor thrust and moments) and the tip vortex strength harmonics is required. For that purpose, throughout the discussion in this section, for a counter-clockwise rotating rotor ψ is consider positive and for a clockwise rotating rotor ψ is consider to be negative (wherever \pm appears, “+” stands for $\psi > 0$ and “-” stands for $\psi < 0$)

The tip vortex variation is first defined using both $\psi_1 (= \Omega t)$ and ψ_n as:

$$\tilde{\Gamma}_{\text{tip}}(n, \psi_1) = \tilde{\Gamma}_{\text{trim}}(\psi_n) + \Delta\tilde{\Gamma}_0(\psi_1) + \Delta\tilde{\Gamma}_{1s}(\psi_1) \sin(\psi_n) + \Delta\tilde{\Gamma}_{1c}(\psi_1) \cos(\psi_n), \quad (3)$$

where $\tilde{\Gamma}_{\text{tip}}(n, \psi_1)$ is the n -th blade tip vortex at time $t = \psi_1/\Omega$ when the blade is located at $\psi_n (= \psi_1 + \frac{2\pi(n-1)}{N_b})$. The periodic function $\tilde{\Gamma}_{\text{trim}}(\psi)$ represents the tip vortex at the trim state (e.g., in pure hover $\tilde{\Gamma}_{\text{trim}}(\psi)$ is constant), and $\Delta\tilde{\Gamma}_0, \Delta\tilde{\Gamma}_{1s}, \Delta\tilde{\Gamma}_{1c}$ are the tip vortex perturbations due to $\Delta C_T, \Delta C_L, \Delta C_M$.

To evaluate the relations between the time histories of $\Delta C_T, \Delta C_L, \Delta C_M$ and the time histories of $\Delta\tilde{\Gamma}_0, \Delta\tilde{\Gamma}_{1s}, \Delta\tilde{\Gamma}_{1c}$, the perturbation of the bound vortex along the blade is assumed to be related to the perturbation of the tip vortex magnitude as

$$\Delta\tilde{\Gamma}_B(n, \tilde{r}, \psi_1) = F(\tilde{r}) \left[\tilde{\Gamma}_{\text{tip}}(n, \psi_1) - \tilde{\Gamma}_{\text{trim}}(\psi_n) \right], \quad (4)$$

where $F(\tilde{r})$ is a nondimensional shape function of \tilde{r} , normalized so that $F_{\text{max}} = 1$. Using $\tilde{U}(\tilde{r}, \psi) = \tilde{r} \pm \mu \sin(\psi)$, one may write

$$\begin{aligned} [\Delta C_T, \Delta C_L, \Delta C_M](\psi_1) = & \quad (5) \\ \frac{1}{\pi} \sum_{n=1}^{N_b} \int_0^1 \tilde{U}(\tilde{r}, \psi_n) \Delta\tilde{\Gamma}_B(n, \tilde{r}, \psi_1) & \\ [1, -\tilde{r} \sin(\psi_n), -\tilde{r} \cos(\psi_n)] d\tilde{r}. & \end{aligned}$$

Hence, $\Delta C_T, \Delta C_L, \Delta C_M$ turn to be linear functions of $\Delta\tilde{\Gamma}_0, \Delta\tilde{\Gamma}_{1s}, \Delta\tilde{\Gamma}_{1c}$. By integrating and inverting these relations one may write:

$$\Delta\tilde{\Gamma}_0 = \gamma_1 \frac{\pi}{N_b} \frac{\Delta C_T \pm \gamma_2 \mu \Delta C_L}{1 - \gamma_3 \mu^2} \quad (6a)$$

$$\Delta\tilde{\Gamma}_{1s} = -\gamma_4 \frac{\pi}{N_b} \frac{\Delta C_L \pm \frac{1}{2} \mu \Delta C_T}{1 - \gamma_3 \mu^2} \quad (6b)$$

$$\Delta\tilde{\Gamma}_{1c} = -\gamma_4 \frac{\pi}{N_b} \Delta C_M. \quad (6c)$$

Figure 4 presents typical $F(\tilde{r})$ functions and their γ_i coefficients (cases I and IV are given just as reference values). As shown, the variation

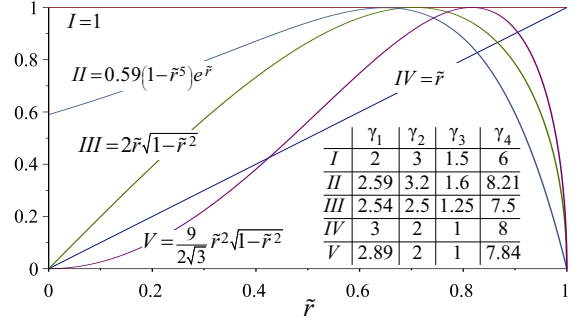


Fig. 4 Various $F(\tilde{r})$ functions and their influence on γ_i .

in these coefficient is quite narrow and so their influence on the results presented in what follows. Function II of Fig. 4 was subsequently used throughout the present analysis. It should be emphasized that the function $F(\tilde{r})$ is used for distributing the perturbational bound vorticity only, while the fundamental distribution is determined by the trim solution. One may claim that the accuracy of the above modelling may be somewhat increased by using the exact distribution of the bound vortex (perturbation) shape, however, such modelling tends to be a “configuration-dependent” one, which contradicts the objective of the present methodology.

Consequently, using Eqs.(6a-c), we are able to apply periodic time histories of frequency ω to $\Delta C_T, \Delta C_L, \Delta C_M$ that will excite the wake through the periodic behavior of $\tilde{\Gamma}_0, \tilde{\Gamma}_{1s}, \tilde{\Gamma}_{1c}$ (at the same frequency).

3.2 Determination of the Inflow States

As already stated, the states defined in Eq. (2) are different from the classical as they represent instantaneous inflow distribution over the blades, while the classical ones (see Refs.[1]) are obtained by integration over the rotor disc.

The present analysis exploits the Multi-Blade Coordinate Transformation (also referred to as the Fourier Coordinate Transformation), in a similar way it is used to integrate the dynamics of individual blades and express it in a fixed (nonrotating) frame. Among other applications, the Multi-Blade Coordinate Transformation is mostly used for modal and stability analyses and state-space-based controls design. In the present context, and in order to enable direct comparison with previous studies, we shall ignore the “differential mode” (that appears when the number of blades is even). Subsequently, at each instance, the above three inflow states, $\lambda_0, \lambda_{1s}, \lambda_{1c}$ are determined by the following (exact) weighted integration (valid for $N_b \geq 3$):

$$[\lambda_0, \lambda_{1s}, \lambda_{1c}](\psi_1) = \frac{1}{N_b} \sum_{n=1}^{N_b} \int_0^1 \Delta \tilde{v}_i(\psi_1, \tilde{r}, \psi_n) \times [1, (4+2k)\tilde{r}^k \sin(\psi_n), (4+2k)\tilde{r}^k \cos(\psi_n)] d\tilde{r}, \quad (7)$$

where $k > 0$ is an arbitrary integer and \tilde{r}^k serves as a weighting function ($k = 1$ is typically used). Note again that a blade may experience different induced velocity when it passes the same azimuthal station in various times depending on the inflow states values at the corresponding times.

Figure 5 presents the time history of the inflow coefficients in hover due to three perturbations of $\Delta C_T, \Delta C_L, \Delta C_M$ (one at a time). As shown, in hover, ΔC_T mainly excites λ_0 , and $\Delta C_L, \Delta C_M$ mainly excite $\lambda_{1s}, \lambda_{1c}$, respectively. On

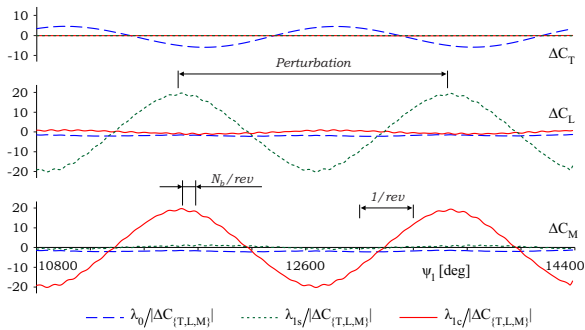


Fig. 5 $\lambda_0, \lambda_{1s}, \lambda_{1c}$ due to $\Delta C_T, \Delta C_L, \Delta C_M$ (Hover, $\tilde{\omega} = 0.2, N_b = 4$).

the other hand as shown in Fig. 6, in forward flight, a clear coupling is observed in the form

of λ_{1c} due to C_T and λ_0 due to C_M . It is also shown, that the perturbation frequency overshadows other fluctuations of higher frequencies (and lower magnitudes). The visible small fluctuations in Fig. 6 are of N_b/rev . frequency.

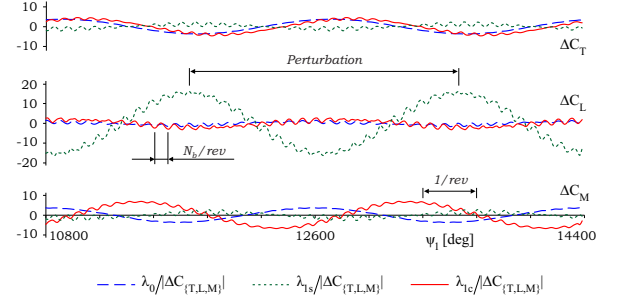


Fig. 6 $\lambda_0, \lambda_{1s}, \lambda_{1c}$ due to $\Delta C_T, \Delta C_L, \Delta C_M$ ($\mu = 0.2, \tilde{\omega} = 0.2, N_b = 4$).

3.3 Inflow Dynamics in Hover

Inflow dynamics, along with the associated Bode plots for hover have been presented and discussed in Refs.[12] (and will be shown again further on). Yet, it is interesting to examine the associated inflow distributions due to the loading distributions that are obtained in this case.

Figure 7 presents the inflow distribution in hover for four-bladed rotor when the perturbation is given by $\Delta C_L = C_L^c \cos(\omega t)$ (and no other perturbations are applied) at a moment that is relatively easy to analysed. This is done for a case when the perturbation frequency may be written as rational number, namely $\tilde{\omega} = \frac{n}{m}$. In such a case, after n perturbation revolutions the rotor completes m revolutions and at that instance, the ΔC_L perturbation is maximal: Blade#1 is at $\psi = 0$ and (for four bladed rotor) and Blades#2,3 and 4 are located at $\psi = 90^\circ, 180^\circ, 270^\circ$, respectively. At such an instance, according to Eq.(6b), the perturbation in tip circulation magnitude is minimal and hence, the inflow over Blade#2 is reduced. As shown, the perturbation is well approximated by Eq.(7) within the basic assumption of a linear variation.

3.4 Inflow Dynamics in Forward Flight

In this section we shall study the dynamic inflow characteristics obtained in forward flight as de-

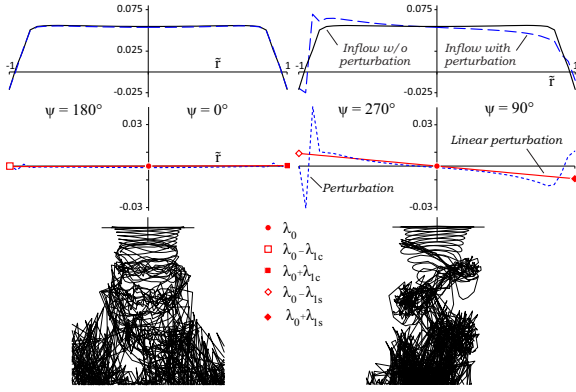


Fig. 7 Lateral and longitudinal inflow distributions due to $\Delta C_L = 0.0005 \cos(\tilde{\omega}\psi_1)$ when perturbation is maximal and Blade#1 is at $\psi_1 = 0$ (Hover, $\tilde{\omega} = 0.2$, $C_T = 0.005$, $N_b = 4$).

scribed by Eq. (1), Fig. 3 and the related discussion. Figure 8 shows several wake structures obtained by applying pitch moment perturbations of various rates. The wake response is clearly demonstrated, where the distance between the periodic structures is given by $\frac{d}{R} = 2\pi \frac{\mu}{\tilde{\omega}}$.

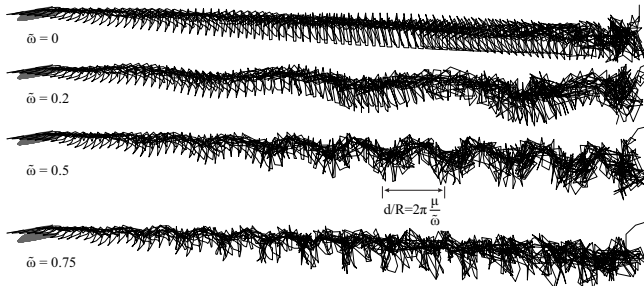


Fig. 8 Wake structure during various rates of pitch moment in forward flight ($C_T = 0.005$, $\mu = 0.2$).

Figure 9 presents the inflow distribution in forward flight when the ΔC_T perturbation is maximal and Blade#1 is at $\psi_1 = 0$ (similar to the case of Fig. 7). As shown, the perturbation creates both λ_0 and λ_{1c} response with a smaller influence on λ_{1s} .

In a similar way, Fig. 10 presents the inflow distribution in forward flight when the ΔC_L perturbation is maximal. As shown, the perturbation induces upwash (negative downwash) on the advancing blade and downwash on the retreating blade with negligible influence on the downwash mean value and the distribution over the longitudi-

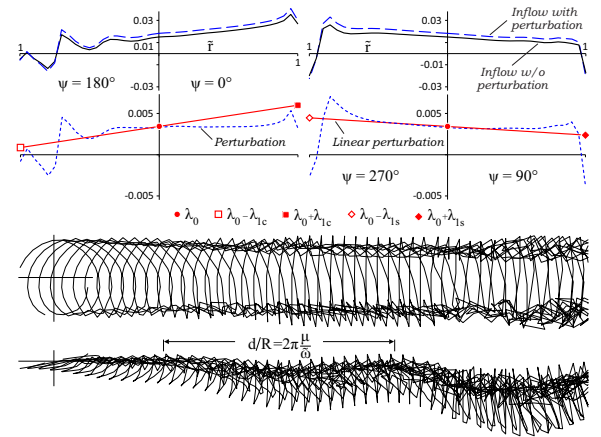


Fig. 9 Lateral and longitudinal inflow distributions due to $\Delta C_T = 0.001 \cos(\tilde{\omega}\psi_1)$ when the perturbation is maximal and Blade#1 is at $\psi_1 = 0$ ($\mu = 0.2$, $\tilde{\omega} = 0.2$, $C_T = 0.005$, $N_b = 4$)

dinal plane. The lateral geometric changes in the wake over the length $\frac{d}{R} = 2\pi \frac{\mu}{\tilde{\omega}}$ are also visible.

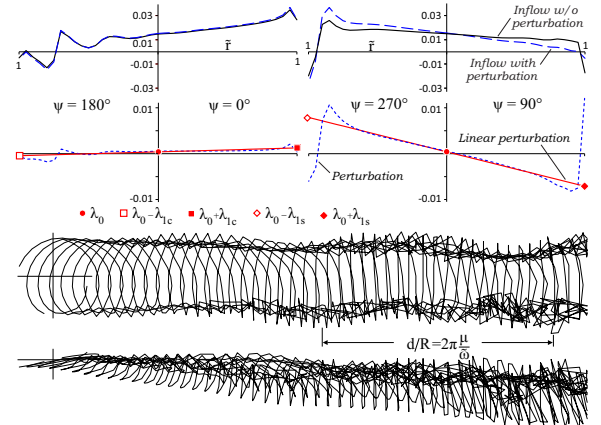


Fig. 10 Lateral and longitudinal inflow distributions due to $\Delta C_L = 0.0005 \cos(\tilde{\omega}\psi_1)$ when perturbation is maximal and Blade#1 is at $\psi_1 = 0$ ($\mu = 0.2$, $\tilde{\omega} = 0.2$, $C_T = 0.005$, $N_b = 4$)

The case where the ΔC_M perturbation is introduced is shown in Fig. 11. Here, a clear coupling with the downwash mean value is shown, while the lateral distribution is hardly influenced, and the longitudinal variation tends to increase inflow over blade#3 (at $\psi = 180^\circ$).

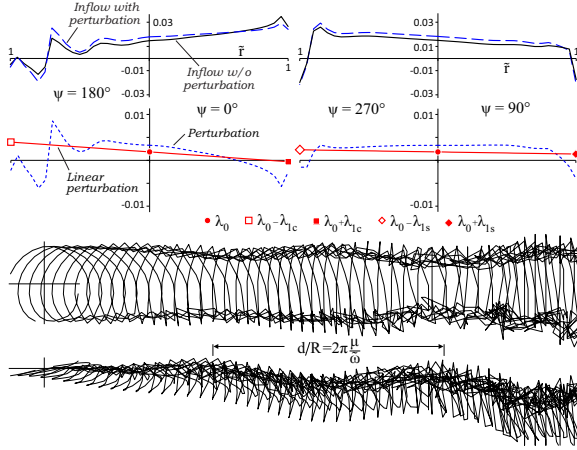


Fig. 11 Lateral and longitudinal inflow distributions due to $\Delta C_M = 0.0005 \cos(\bar{\omega}\psi_1)$ when perturbation is maximal and Blade#1 is at $\psi_1 = 0$ ($\mu = 0.2$, $\bar{\omega} = 0.2$, $C_T = 0.005$, $N_b = 4$)

3.5 Bode Plots

Figures 12-14 show the Bode plot for $\Delta C_T, \Delta C_L, \Delta C_M$ perturbations. In general, both magnitudes and phase angles are decreasing with speed. Solid lines represent the state-space results and symbols are the actual values obtained by the free-wake analysis for $C_T = 0.005$, $N_b = 4$, $\alpha_D = 10^\circ$.

Figure 12 shows the λ_0 due to ΔC_T response. It is evident that for low and median frequencies, the state-space model constitutes an excellent approximation with relatively small discrepancies for higher frequencies. Figure 13 shows the “on

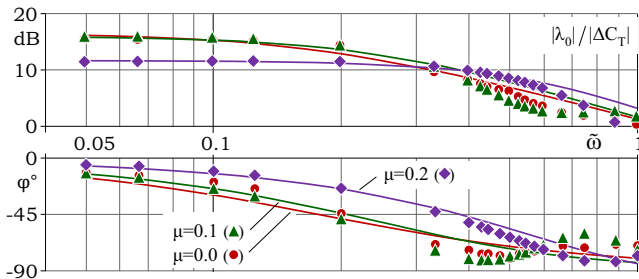


Fig. 12 λ_0 due to ΔC_T response.

axis” response of λ_{1s} due to ΔC_L and λ_{1c} due to ΔC_M . Good matching between the state-space model and the free-wake analysis is obtained for λ_{1s} due to ΔC_L while unlike the hover case (see correlation for $\mu = 0$), discrepancies are observed

for the low frequency region of the λ_{1c} due to ΔC_M response in forward flight. Hence, in forward flight, and as opposed to the case of periodic roll motion, the pitch response that emerges from the fundamental first order system hypothesis is more questionable. One may assume that

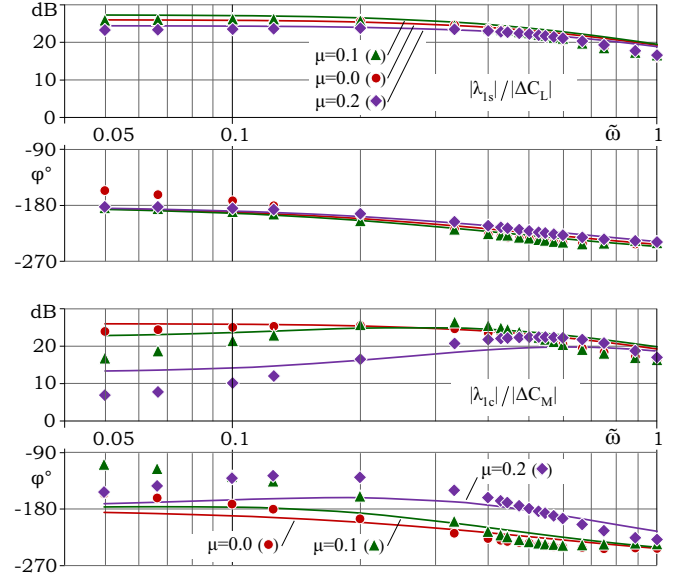


Fig. 13 λ_{1s} due to ΔC_L response and λ_{1c} due to ΔC_M response.

this phenomena is related to the fact that in forward flight, roll moment perturbations are superimposed on relatively symmetric wake structure (right vs. left disc areas), while pitch moment perturbations are superimposed on a wake which is substantially skewed and not symmetric (forward vs. backwards disc areas) as also indicated by the longitudinal inflow distribution in Fig. 11.

Figure 14 presents the coupling terms λ_{1c} due to ΔC_T and λ_0 due to ΔC_M in forward flight. The free-wake results in this case exhibit the general trend of the state-space approximation mainly in the low frequencies region.

It should be noted that a study of the influence of the number of blades has shown that this parameter has very limited effect on the above results.

4 Inflow Dynamics for Maneuvering Flight

Dynamic Inflow influence on maneuvering flight has been in the focus of a considerable body of

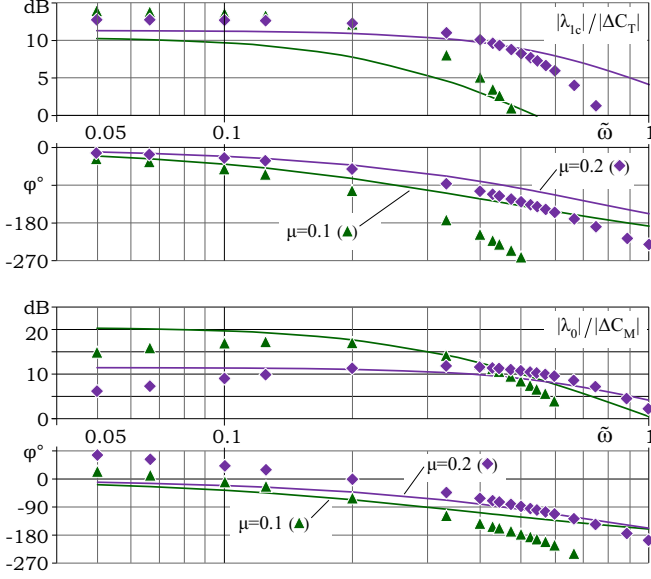


Fig. 14 λ_{1c} due to ΔC_T response and λ_0 due to ΔC_M response.

research, see e.g. Refs.[21-22]. Within this section, we shall describe an extension of the above methodology for predicting the inflow dynamics in the case of heaving, rolling and pitching rotor disc.

Similar to the classical dynamic inflow hypothesis shown in Eq. (1), we have explored the inflow dynamics due to heaving, rolling and pitching by the first-order system

$$[M^D] \begin{pmatrix} \lambda_0^* \\ \lambda_{1s}^* \\ \lambda_{1c}^* \end{pmatrix} + [L^D]^{-1} \begin{pmatrix} \lambda_0 \\ \lambda_{1s} \\ \lambda_{1c} \end{pmatrix} = \begin{pmatrix} \tilde{w}_D \\ \tilde{p}_D \\ \tilde{q}_D \end{pmatrix}, \quad (8)$$

where in the above, \tilde{w}_D is the vertical (heaving, normalized by ΩR) motion velocity while \tilde{p}_D and \tilde{q}_D are the total disc roll and pitch tilt rates (normalized by Ω) that might include components of $-\beta_{1s}^*$ and $-\beta_{1c}^*$, respectively.

Figure 15 is an example for the wake structure during pitch motion of various amplitudes. The periodic nature of the wake is clearly observed.

To evaluate the elements of the matrices $[M^D]$ and $[L^D]$, we have used the procedure shown in Fig. 16 which is almost identical to the one described above in Fig. 3. In this case the elements of the matrices $[M^D]$ and $[L^D]$ are de-

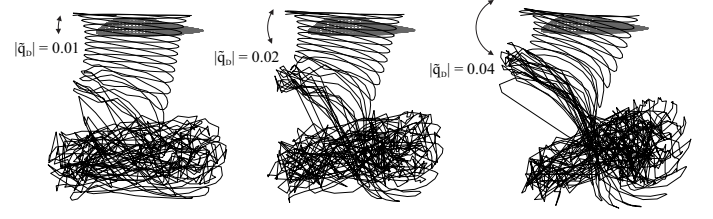


Fig. 15 Wake structure during pitch motion (Hover, $\tilde{\omega} = 0.1$, $C_T = 0.005 N_b = 4$).

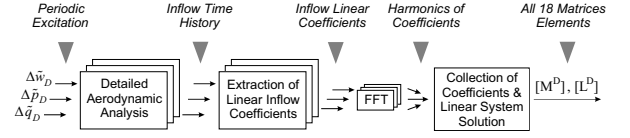


Fig. 16 Scheme of the *Single frequency analysis* methodology for a single rotor system in maneuvering flight.

termined by applying the periodic perturbations $\Delta \tilde{w}_D(\psi_1)$, $\Delta \tilde{p}_D(\psi_1)$ and $\Delta \tilde{q}_D(\psi_1)$.

As shown in Fig. 15, in our present model, the disc is assumed to move and tilt relative to the “wind axes” while the induced velocity $\Delta \tilde{v}_i(\psi_1, \tilde{r}, \psi)|_{wind}$ is determined at these “wind axes” by applying Biot-Savart law at each instance. Yet, the flapping equations require the induced velocity over a stationary assumed disc. Hence, the nondimensional induced velocity in these “disc axes” is therefore:

$$\Delta \tilde{v}_i(\psi_1, \tilde{r}, \psi) = \Delta \tilde{v}_i(\psi_1, \tilde{r}, \psi)|_{wind} - \tilde{w}_D(\psi_1) + \tilde{q}_D(\psi_1) \tilde{r} \cos(\psi) + \tilde{p}_D(\psi_1) \tilde{r} \sin(\psi) \quad (9)$$

or

$$\begin{aligned} \lambda_0 &= \lambda_0^{wind} - \tilde{w}_D, \\ \lambda_{1s} &= \lambda_{1s}^{wind} + \tilde{p}_D, \\ \lambda_{1c} &= \lambda_{1c}^{wind} + \tilde{q}_D. \end{aligned} \quad (10)$$

The above linear inflow coefficients (λ_0 , λ_{1s} , λ_{1c}) are those that have to be used in the flapping equations.

As already explained, the procedure described in Fig. 16 was utilized with the periodic perturbations of $\Delta \tilde{w}_D(\psi_1)$, $\Delta \tilde{p}_D(\psi_1)$ and $\Delta \tilde{q}_D(\psi_1)$. Figure 17(a) shows the resulting diagonal terms of the $[M^D]$ matrix as obtained for various frequencies. Apparently, these values are

not constant and violate the basic assumption embedded in Eq. (8). However, in the disc plan, the flapping time dependent equations are driven by the quantities $(\lambda_0 + \tilde{w}_D)$ for the heave motion, $(\lambda_{1s} - \tilde{p}_D)$ for the roll motion and $(\lambda_{1c} - \tilde{q}_D)$ for the pitch motion. Hence, when Eq. (8) is constructed by the time histories of $\lambda_0^{wind} = \lambda_0 + \tilde{w}_D$, $\lambda_{1s}^{wind} = \lambda_{1s} - \tilde{p}_D$ and $\lambda_{1c}^{wind} = \lambda_{1c} - \tilde{q}_D$ (as opposed to λ_0 , λ_{1s} and λ_{1c} , respectively) the diagonal terms shown in Fig. 17(b) are obtained. As demonstrated, these are fairly constant values that may serve (after suitable averaging) as a basis for a state-space model that may be directly used by the flapping equations.

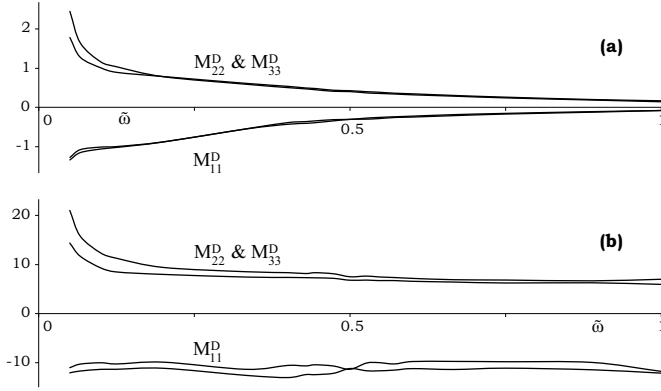


Fig. 17 The diagonal terms of the $[M^D]$ matrix vs. frequency: (a) The case of λ_0 , λ_{1s} , λ_{1c} . (b) The case of $(\lambda_0 + \tilde{w}_D)$, $(\lambda_{1s} - \tilde{p}_D)$ and $(\lambda_{1c} - \tilde{q}_D)$ ($C_T = 0.005$, $N_b = 4$).

The corresponding Bode plot appears in Fig. 18. Note that the two sets of data shown in the figures of this section represent different values of perturbation amplitudes ($\tilde{w}_D, \tilde{p}_D, \tilde{q}_D = 0.01, 0.02$) which testify for the generalized nature of the results with that respect.

The general conclusion that emerges from the above discussion is that one may only evaluate the (first-order system) response of $\lambda_0 + \tilde{w}_D$, $\lambda_{1s} - \tilde{p}_D$ and $\lambda_{1c} - \tilde{q}_D$ and use these directly to activate the flapping equations.

The evaluation of a simplified “wake curvature coefficient”, K_r , from the above analysis may be done in various ways since as shown above, the whole concept of a frequency independent (“steady”) relation of $\lambda_{1c} = K_r \tilde{q}_D$ where K_r is a constant is not accurate. One way to look at K_r ,

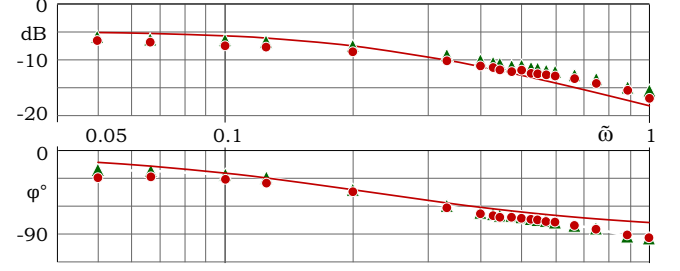


Fig. 18 Bode plot for the state-space approximation (solid line) and the free-wake results (symbols) $\lambda_{1c} - \tilde{q}_D$ due to \tilde{q}_D (and $\lambda_{1s} - \tilde{p}_D$ due to \tilde{p}_D) ($C_T = 0.005$, $N_b = 4$).

(or its extension to K_p, K_q as the wake curvature coefficients in roll and pitch, respectively, and K_w as the “wake stretching coefficient”) is to ignore the matrix $[M^D]$ and all the off-diagonal terms of $[\bar{L}^D]$. This leads to $\lambda_{1s} = \frac{\tilde{p}_D}{\bar{L}_{22}^D}$ or $K_p = 1/\bar{L}_{22}^D$ and similarly, $K_q = 1/\bar{L}_{33}^D$ and $K_w = 1/\bar{L}_{11}^D$.

Figure 19 shows the frequency response of the above coefficients. Evidently, for low frequency, $K_p = K_q = -K_w \cong 1.5$, a value that is reduced to about 1.0 for high frequencies.

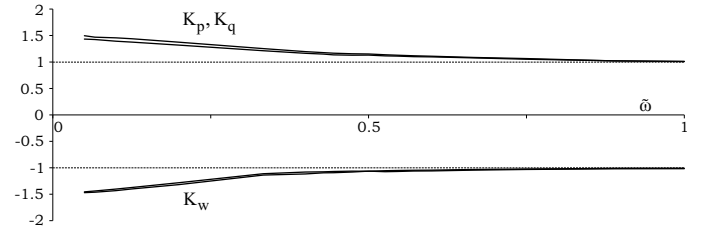


Fig. 19 Frequency response of the wake curvature coefficients (K_p, K_q) and the wake stretching coefficient (K_w).

5 Coaxial-Rotor Analysis

Similar to the hypotheses embedded in Eq. (1), for a coaxial rotor, the inflow dynamics is written

as the following first order system:

$$[M] \begin{Bmatrix} \lambda_0^U \\ \lambda_{1s}^U \\ \lambda_{1c}^U \\ \lambda_0^L \\ \lambda_{1s}^L \\ \lambda_{1c}^L \end{Bmatrix} + [\bar{L}] \begin{Bmatrix} \lambda_0^U \\ \lambda_{1s}^U \\ \lambda_{1c}^U \\ \lambda_0^L \\ \lambda_{1s}^L \\ \lambda_{1c}^L \end{Bmatrix} = \begin{Bmatrix} \Delta C_T^U \\ \Delta C_L^U \\ \Delta C_M^U \\ \Delta C_T^L \\ \Delta C_L^L \\ \Delta C_M^L \end{Bmatrix}, \quad (11)$$

where superscript U and L represents the upper and the lower rotors, respectively. The matrices $[M]$ and $[\bar{L}]$ have the following structure:

$$[M] \equiv \begin{bmatrix} [M_{UU}] & [M_{UL}] \\ [M_{LU}] & [M_{LL}] \end{bmatrix}; [\bar{L}] \equiv \begin{bmatrix} [\bar{L}_{UU}] & [\bar{L}_{UL}] \\ [\bar{L}_{LU}] & [\bar{L}_{LL}] \end{bmatrix}, \quad (12)$$

where $[M_{UU}]$ and $[\bar{L}_{UU}]$ represent the influence of the Upper rotor on itself; $[M_{LL}]$ and $[\bar{L}_{LL}]$ represent the influence of the Lower rotor on itself; $[M_{UL}]$ and $[\bar{L}_{UL}]$ represent the influence of the Upper rotor on the Lower rotor and $[M_{LU}]$ and $[\bar{L}_{LU}]$ represent the influence of the Lower rotor on the Upper rotor.

For a coaxial rotor system, two new nondimensional parameters are introduced: The clearance between the rotors, H , in terms of H/D , and the system thrust sharing ratio, T^L/T^U , that is taken from the basic trim solution that is performed prior to the dynamic inflow extraction (similar to the case of a single rotor system). Subsequently, the H/D and T^L/T^U ratios are treated as independent parameters.

5.1 Calculating the $[M]$ and $[\bar{L}]$ Matrices for a Coaxial Rotor

Along the lines of the single rotor analysis, perturbational loads are the drivers of the analysis in the case of a coaxial rotor system as well. Subsequently, we apply periodic perturbations to both rotors, one perturbation at the time, at a given frequency, ω , e.g. ΔC_T^U , of the type:

$$\Delta C_T^U = C_T^{sU} \sin(\omega t) + C_T^{cU} \cos(\omega t). \quad (13)$$

Figure 20 summarizes the methodology in this case which is essentially based on doubling

the process by introducing $\Delta C_T^U(\psi_1)$, $\Delta C_L^U(\psi_1)$, $\Delta C_M^U(\psi_1)$ periodic perturbations in addition to $\Delta C_T^L(\psi_1)$, $\Delta C_L^L(\psi_1)$, $\Delta C_M^L(\psi_1)$ perturbations. The

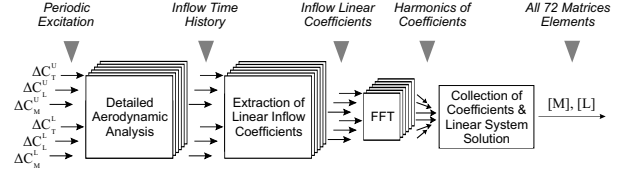


Fig. 20 Scheme of the *Single frequency analysis* methodology for a coaxial rotor system.

definition of induced velocity over each rotor is similar to Eq. (2) and so the methodology of extraction the linear variation from the actual inflow distribution described in Eq. (7). Yet, to avoid confusion and to eliminate the need to deal with two opposite azimuth angles of the two rotors, we have defined the linear inflow variation over the lower rotor by the *upper rotor* azimuth angle (ψ_U):

$$\Delta \tilde{v}_i^U(\psi_1, \tilde{r}, \psi) \quad (14)$$

$$= \lambda_0^U(\psi_1) + \lambda_{1s}^U(\psi_1) \tilde{r} \sin(\psi_U) + \lambda_{1c}^U(\psi_1) \tilde{r} \cos(\psi_U),$$

$$\Delta \tilde{v}_i^L(\psi_1, \tilde{r}, \psi) \quad (15)$$

$$= \lambda_0^L(\psi_1) + \lambda_{1s}^L(\psi_1) \tilde{r} \sin(\psi_U) + \lambda_{1c}^L(\psi_1) \tilde{r} \cos(\psi_U).$$

Using this notation, $\lambda_{1s}^U > 0$ indicates increased inflow over the upper rotor disc at the $\psi_U = 90^\circ$ area, while $\lambda_{1s}^L > 0$ indicates increased inflow over the lower rotor disc *at the area below* $\psi_U = 90^\circ$. Such definitions simplify the examination of the physical phenomena as it views both disc in a similar way.

Figure 21 shows the upper and the lower rotor wakes and their interactions in hover. As demonstrated, the wakes interact and both wakes induce velocity on both disc plans.

5.2 System Characteristics

The $[M]$ and $[\bar{L}]$ obtained for a coaxial rotor system enable several “sanity” checks that were executed and proven to be true. The following is written for the $[\bar{L}]$ matrix but holds also for the $[M]$ matrix as well:

(a) For infinite clearance:

$$[\bar{L}_{UU}] = [\bar{L}_{LL}] = [\bar{L}]_{\text{Single}}$$

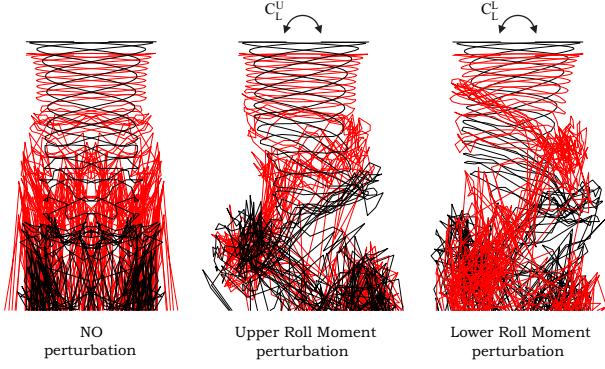


Fig. 21 The upper and the lower rotor wakes in hover: No perturbation; Roll perturbation in the upper rotor; Roll perturbation in the lower rotor.

$$[\bar{L}_{UL}] = [\bar{L}_{LU}] = [0].$$

(b) For zero clearance:

$$\begin{aligned} [\bar{L}_{UU}] &= [\bar{L}_{LL}] \neq [\bar{L}]|_{\text{Single}} \\ [\bar{L}_{UL}] &= [\bar{L}_{LU}] \neq [0]. \end{aligned}$$

(c) For finite (practical, see Fig. 22 below) clearance:

$$\begin{aligned} [\bar{L}_{UU}] &\neq [\bar{L}_{LL}] \neq [\bar{L}]|_{\text{Single}} \\ [\bar{L}_{UL}] &\neq [\bar{L}_{LU}]. \end{aligned}$$

Figure 22 presents typical coaxial matrices compared with those of single rotor system in hover. First note that in this hover case, many of terms vanish. It is also shown that $[\bar{L}_{11}]$, $[\bar{L}_{14}]$, $[\bar{L}_{41}]$ and $[\bar{L}_{44}]$ dominate in magnitude as they are related to the rotors' thrust, similar to the $[\bar{L}_{11}]$ term for a single rotor. Similar trend is observed for the corresponding terms of $[M]$.

5.3 Bode Plots in Hover

Figure 23 presents the bode plot for λ_0^U and λ_0^L due to ΔC_T^U and ΔC_T^L . Symbols represent the free wake results while lines show the state-space approximation. As shown, the behavior of λ_0^U due to ΔC_T^U is very similar to the behavior of λ_0 due to ΔC_T for a single rotor shown in Fig. 12. As expected, λ_0^U due to ΔC_T^L is lower due to the fact that the upper rotor is placed above (and out of) the lower rotor wake. On the other hand λ_0^L due to ΔC_T^U and λ_0^L due to ΔC_T^L are similar in magnitude.

	Single	Coaxial	
$[M]$	$\begin{bmatrix} 0.848 & & \\ & -0.097 & \\ & & -0.097 \end{bmatrix}$	$\begin{bmatrix} 1.069 & -0.574 \\ -0.123 & 0.039 \\ -0.406 & 0.039 \end{bmatrix}$	$\begin{bmatrix} 0.011 & 1.015 \\ 0.011 & -0.109 \\ & -0.109 \end{bmatrix}$
$[\bar{L}]$	$\begin{bmatrix} 0.150 & & \\ & -0.050 & \\ & & -0.050 \end{bmatrix}$	$\begin{bmatrix} 0.515 & -0.407 \\ -0.079 & 0.031 \\ -0.550 & 0.659 \end{bmatrix}$	$\begin{bmatrix} 0.031 & 0.031 \\ -0.079 & 0.031 \\ 0.100 & -0.091 \\ 0.100 & -0.091 \end{bmatrix}$

Fig. 22 The matrices $[M]$ and $[\bar{L}]$ for coaxial rotor system in hover, $H/D = 0.1$, $T^L/T^U = 1.0$, $C_T^U + C_T^L = 0.01$, compared with single rotor system matrices for $C_T = 0.005$.

Note that the above observation regarding the similarity of the behavior of λ_0^U due to ΔC_T^U and the behavior of λ_0 due to ΔC_T for a single rotor occurs despite the fact that the relevant matrices in Fig. 22 are clearly different. For example, replacing $[\bar{L}_{UU}]$ and $[\bar{L}_{LL}]$ with $[\bar{L}]$ of a single rotor in addition to setting $[\bar{L}_{UL}] = [\bar{L}_{LU}] = [0]$ is *not* an acceptable approximation at all. It is evident that in this case, the off diagonal matrices $[\bar{L}_{UL}]$, and $[\bar{L}_{LU}]$ play a major role.

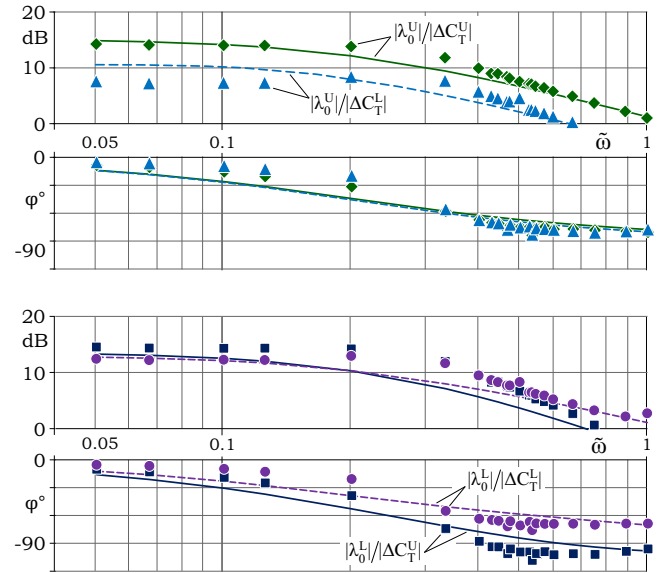


Fig. 23 Bode plot of λ_0^U and λ_0^L due to ΔC_T^U and ΔC_T^L (Hover, $H/D = 0.1$, $T^L/T^U = 1.0$, $C_T^U + C_T^L = 0.01$).

In addition, Fig. 24 presents the bode plot for λ_{1s}^U and λ_{1s}^L due to ΔC_L^U and ΔC_L^L (similar plot may be drawn for λ_{1c} and ΔC_M of both rotors). As

shown, the moments over the upper rotor induce similar perturbations over both rotor plans due to the fact that the lower rotor is placed below (and mostly within) the upper rotor wake, while the moments over the lower rotor induce larger perturbation over the lower rotor than over the upper rotor, again due to the fact that the upper rotor is placed above (and out of) the lower rotor wake.

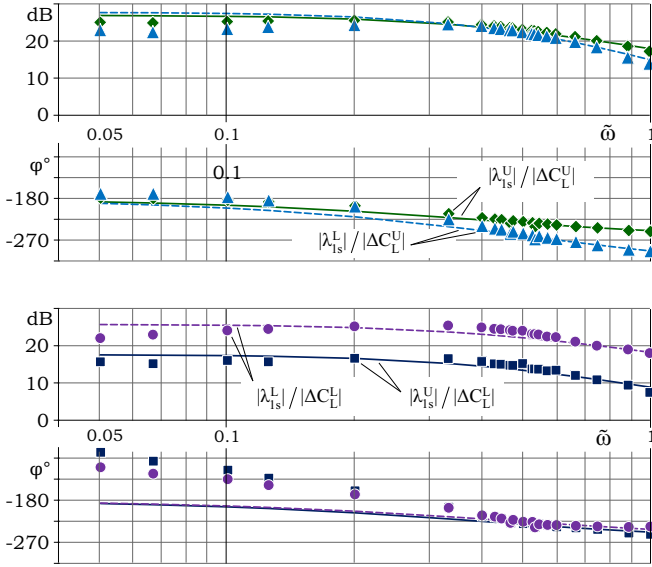


Fig. 24 Bode plot of λ_{1s}^U and λ_{1s}^L due to ΔC_L^U and ΔC_L^L (Hover, $H/D = 0.1$, $T^L/T^U = 1.0$, $C_T^U + C_T^L = 0.01$).

5.4 Forward Flight

A general view of the wake structure of a coaxial rotor system in forward flight in the rotor vicinity is shown in Fig. 25. Careful examination of the wake geometry with and without perturbation shows that unlike the hover case shown in Figure 21, the mutual modifications in the wake structures in the rotor vicinity are negligible. Similar to the case of a single rotor, even for very slow forward speed, the free stream velocity carries the wake away from the rotor in such a manner that the main interference between the rotors lies mainly in the mutual velocities induced by the time varying magnitudes of the tip vortices.

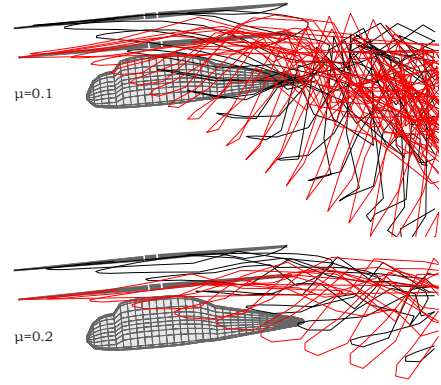


Fig. 25 Upper and lower wake structures in forward flight ($H/D = 0.1$, $T^L/T^U = 0.9$).

6 Conclusion

A methodology for extracting linearized state-space dynamic inflow model from high fidelity aerodynamic analysis for various helicopter rotor systems in all flight regimes is offered. The methodology is also extended to the case where dynamic inflow model is required for maneuvering flight.

The present methodology employs a *Single frequency analysis* procedure and is different from the classical one in two ways: First, the methodology may employ any high fidelity aerodynamic modeling. Such models have far fewer limitations and represent the state-of-the-art in rotorcraft aerodynamic modeling. Hence, the outcome ought to be of higher quality. The second difference is the definition of the “inflow states” that is different from the classical one. The states defined in this study are “exact” in the sense that they are directly related (only) to the inflow distribution along each blade at each instant. Hence, these states may adequately represent any rate of inflow dynamics and are directly relevant to the instantaneous load estimation required during real time simulations. This feature is of high importance in maneuvering flight.

The analysis is completely a non-dimensional one and deals only with global thrust and moments over the rotors. Additional advantage of the present methodology lies in the fact that there is a complete separation between the inflow analysis and loads evaluation.

The results demonstrate that the *Single fre-*

quency analysis methodology is capable of direct calculations of all involved state-space coefficients within the first-order hypothesis of the dynamic inflow model. The methodology determines the coefficients per given frequency (18 coefficients for the single case and 72 coefficients for the coaxial case) while uniformity over the relevant frequency range testifies to the level of validity of the basic first-order system hypothesis.

In general, for a single rotor, the results show similarity to the classical results and indicate regions where the basic hypothesis is less applicable. It is also shown that the rotor response to heaving, rolling and pitching motion may be described as a first order as well.

For a coaxial rotor system in hover, it is shown that in general, the basic hypothesis of first-order system behavior holds as well in most of the cases with some exceptions. The associated matrices demonstrate the fact that due to the high coupling in the system, the resulting matrices are clearly different from the case of a single rotor.

References

- [1] Pitt, D. M., and Peters, D. A., "Theoretical Prediction of Dynamic Inflow Derivatives", *Vertica*, Vol. 5, No. 1, 1981, pp. 21–34.
- [2] Gaonkar, G.H., Peters, D.A., "Effectiveness of Current Dynamic-Inflow Models in Hover and Forward Flight", *Journal of the American Helicopter Society*, Vol. 31, No. 2, 1 April 1986, pp. 47-57(11).
- [3] Peters, D. A., and HaQuang, N., "Dynamic Inflow for Practical Applications", Technical Note, *Journal of the American Helicopter Society*, Vol. 33, No. 4, Oct 1988, pp. 64-68.
- [4] Peters, D. A., and He, C.-J., "Correlation of Measured Induced Velocities with a Finite-State Wake Model", *Journal of the American Helicopter Society*, Vol. 36, No. 3, July 1991, pp. 59–70.
- [5] Johnson, W. "Feasibility Investigation of General Time-Domain Unsteady Aerodynamics of Rotors", NASA CR 177570, 1990.
- [6] Ellenrieder, T. J., and Brinson, P. R., "The Dynamic Induced Velocity Field of a Model Rotor in Hover Conditions", *The Aeronautical Journal*, Vol. 102, No. 1016, Jun-Jul 1998.
- [7] Bagai, A., Leishman, J.G., Park, J., "Aerodynamic Analysis of a Helicopter in Steady Maneuvering Flight Using a Free-Vortex Rotor Wake Model", *Journal of the American Helicopter Society*, Vol. 44, No. 2, 1 April 1999, pp. 109-120(12).
- [8] Leishman, J. G., Bhagwat, M. J., and Bagai, A., "Free-Vortex Filament Methods for the Analysis of Helicopter Rotor Wakes", *Journal of Aircraft*, Vol. 39, No. 5, September-October 2002, pp. 759–775.
- [9] Bhagwat, M. J., and Leishman, J. G., "Time-Accurate Modeling of Rotor Wakes Using A Free-Vortex Wake Method", *Journal of Aircraft*, Vol. 39, No. 5, September-October 2002, pp. 759–775.
- [10] Rand, O., Khromov, V., "Compound Helicopter: Insight and Optimization", *Journal of the American Helicopter Society*, Vol. 60, No. 1, January 2015, pp. 012001-1–012001-12.
- [11] Joglekar, M., and Loewy, R., "An Actuator-Disc Analysis of Helicopter Wake Geometry and the Corresponding Blade Response", US-AAVLABS Technical Report 69-66, Dec. 1970.
- [12] Rand, O., Khromov, V., Hersey, S., Celi, R., Juhasz, O., and Tischler, M., "Linear Inflow Model Extraction from High-Fidelity Aerodynamic Models for Flight Dynamics Applications", Proceedings of the American Helicopter Society 71st Annual Forum, Virginia Beach, Virginia, May 5-7, 2015.
- [13] Rand, O., Khromov, "Free-Wake Based Dynamic Inflow Model for Hover, Forward and Maneuvering Flight", Proceedings of the American Helicopter Society 72st Annual Forum, West Palm Beach, Florida USA, May 17-19, 2016.
- [14] Rand, O., "RAPiD - Rotorcraft Analysis for Preliminary Design", TAE 987 Report, Technion - Israel Institute of Technology, Faculty of Aerospace Engineering, Haifa, Israel, July 2012.
- [15] Chen, R. T. N., and Hindson, W. S., "Influence of Dynamic Inflow on the Helicopter Vertical Response", NASA TM-88327, June 1986.
- [16] Keller, J.D., "An Investigation of Helicopter Dynamic Coupling Using an Analytical Model",

- Journal of the American Helicopter Society*, Vol. 41, No. 4, 1 October 1996, pp. 322-330(9).
- [17] Prasad, J. V. R., Nowak, M., and Xin, H., “Finite State Inflow Models for a Coaxial Rotor in Hover”, Proceedings of the 38th European Rotorcraft Forum, Amsterdam, Netherlands, 4-7 September 2012.
- [18] Howlett, J.J., “UH-60A Black Hawk Engineering Simulation Program - Vol. II - Background Report”, NASA CR-166310, Dec 1981.
- [19] Curtiss, H.C., “Stability and Control Modeling”, *Vertica*, Vol. 12, No. 4, pp. 381-394, 1988.
- [20] Tischler, M. B. and Remple, R. K., “Aircraft and Rotorcraft System Identification: Engineering Methods with Flight Test Examples”, AIAA, 2nd ed., 2012, Reston, VA.
- [21] Houston, S. S., “Identification of a Coupled Body/Coning/Inflow Model of Puma Vertical Response in the Hover”, *Vertica*, Vol. 13, No. 3, 1989.
- [22] Krothapalli, K.R., Prasad, J.V.R., Peters, D.A., “Helicopter Rotor Dynamic Inflow Modeling for Maneuvering Flight”, Proceedings of the American Helicopter Society 55th Annual Forum, Montreal, Canada, April 1999.

7 Contact Author Email Address

Omri Rand: rand@technion.ac.il

Vladimir Khromov: rapid@technion.ac.il

Copyright Statement

The authors confirm that they, and/or their company or organization, hold copyright on all of the original material included in this paper. The authors also confirm that they have obtained permission, from the copyright holder of any third party material included in this paper, to publish it as part of their paper. The authors confirm that they give permission, or have obtained permission from the copyright holder of this paper, for the publication and distribution of this paper as part of the ICAS proceedings or as individual off-prints from the proceedings.